Graphical Abstract

Role of Atypical Temperature-responsive Lattice Thermal Transport on the Thermoelectric Properties of Antiperovskites Mg_3XN (X = P, As, Sb, Bi)

Jincheng Yue, Yanhui Liu, Wenling Ren, Shuyao Lin, Chen Shen*, Harish Kumar Singh, Tian Cui, Terumasa Tadano, Hongbin Zhang

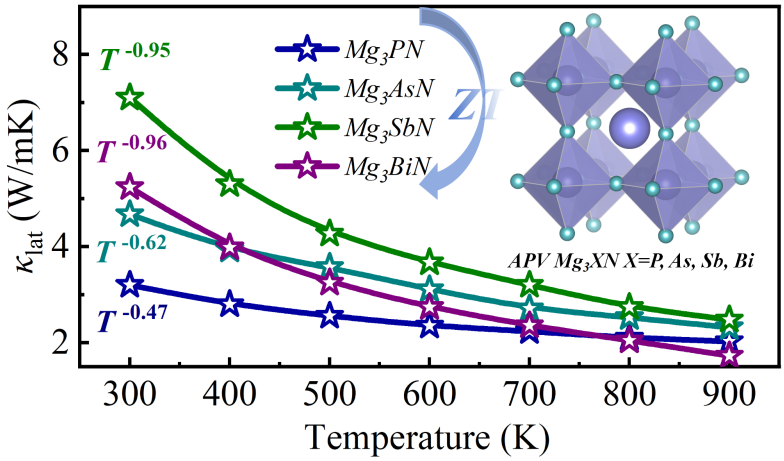

Highlights

Role of Atypical Temperature-responsive Lattice Thermal Transport on the Thermoelectric Properties of Antiperovskites Mg_3XN (X = P, As, Sb, Bi)

Jincheng Yue, Yanhui Liu, Wenling Ren, Shuyao Lin, Chen Shen*, Harish Kumar Singh, Tian Cui, Terumasa Tadano, Hongbin Zhang

- Research highlight 1
  A comprehensive stability evaluation of antiperovskite Mg_3XN with cubic phase is performed, including the thermodynamic, thermal, mechanical, and dynamic stabilities.
- Research highlight 2
  The influence of temperature-responsive lattice thermal conductivity was analyzed based on phonon renormalization and four-phonon scattering.
- Research highlight 3
  The electron-phonon scattering is considered to capture precise carrier mobility and corresponding electronic transport characteristics.
- Research highlight 4
  We predicted the thermoelectric properties of Mg_3XN and confirmed Mg_3BiN as a promising candidate with a theoretical $ZT > 1$.

Role of Atypical Temperature-responsive Lattice Thermal Transport on the Thermoelectric Properties of Antiperovskites Mg_3XN (X = P, As, Sb, Bi)

Jincheng Yue[a], Yanhui Liu[a], Wenling Ren[b], Shuyao Lin[b,c,d], Chen Shen*[b], Harish Kumar Singh[b], Tian Cui[a,e], Terumasa Tadano[f], Hongbin Zhang[b]

[a]*Institute of High Pressure Physics, School of Physical Science and Technology, Ningbo University, Ningbo, 315211, China*
[b]*Institute of Materials Science, Technical University of Darmstadt, Alarich-Weiss-Strasse 2, Darmstadt, 64287, Germany*
[c]*Technische Universität Wien, Institute of Materials Science and Technology, Vienna, A-1060, Austria*
[d]*Linköping University, Department of Physics, Chemistry, and Biology (IFM), Linköping, SE-58183, Sweden*
[e]*State Key Laboratory of Superhard Materials, College of Physics, Jilin University, Changchun 130012, China*
[f]*Research Center for Magnetic and Spintronic Materials, National Institute for Materials and Science, Tsukuba, 350-0047, Japan*

Abstract

Antiperovskite materials have garnered significant attention due to their rich array of physical properties. In this study, we undertake a theoretical exploration into the phase stabilities, and the thermal and electronic transport properties of magnesium-based antiperovskite Mg_3XN (X = P, As, Sb, and Bi) based on density functional theory (DFT) calculations, aiming at designing promising thermoelectric materials. The Mg_3PN and Mg_3AsN possess potential lattice distortion and strong quartic anharmonicity associated with the tilting displacement of Mg_6N octahedra. After phonon renormalization, the thermal conductivity of Mg_3PN and Mg_3AsN exhibits relatively subdued temperature responsiveness with $T^{-0.47}$ and $T^{-0.62}$, respectively. Of note, the thermal conductivity of Mg_3BiN drops the lowest at 900 K because of its distinctive rattle-dominated flat vibrational modes and strong temperature responsiveness with $T^{-0.96}$, despite having a high initial value. Moreover,

Email address: chenshen@tmm.tu-darmstadt.de (Chen Shen*)

the combination of multiple degeneracy pockets and lighter dispersion band edges in Mg_3XN ensures high Seebeck coefficient and impressive electronic conductivity, respectively. Ultimately, Mg_3BiN achieves the optimal power factor, which also guarantees its excellent thermoelectric performance with the ZT values of 1.03 and 1.01 for n-type and p-type at 900 K, respectively. Our findings shed light on the significant impact of unconventional temperature-responsive lattice thermal conductivity on thermoelectric materials for high-temperature applications.

Keywords: Antiperovskite, Four-phonon scattering, Self-consistent phonon theory, Thermoelectric properties, Anharmonic renormalization

1. Introduction

The escalation of energy requisites, fueled by improvements in the overall life quality of human beings, expanding population, and the diminishment of fossil fuel reserves [1–6], presents a complex challenge. Addressing this predicament demands a multifaceted approach, as reliance on af singular source proves inadequate. Consequently, diverse avenues of renewable energy are under scrutiny as potential resolutions to the global energy crisis [7–10]. Thermoelectric (TE) materials with a high figure of merit ZT (ZT=$S^2\sigma/\kappa$, where S, σ, and κ denotes the Seebeck coefficient, electrical conductivity, and thermal conductivity, respectively.) have been attracting significant attention because of potential applications in heat-electricity conversion at high temperatures and cooling around the room temperature [11–13]. Due to the counter-indicative behavior of the Seebeck coefficients and electronic conductivities with respect to the carrier density, it is challenging to optimize the power factor further thus, seeking the relatively independent low lattice thermal conductivity is considered the most feasible option because it facilitates us streamlining complex thermoelectric parameters [14]. Materials with relatively low thermal conductivities, such as chalcogenides [15, 16], oxide perovskites [17, 18], organic compounds [19], skutterudites [20, 21], and Heusler compounds [22, 23], have been investigated as potential candidates for thermoelectric devices that have been explored in recent years.

Since the first antiperovskite (APV) superconductor Ni_3MgC was reported in 2001 [24], such compounds have been studied extensively in the last two decades, and plenty of interesting physical properties and potential functionalities such as magnetic frustration [25], giant magnetoresistances [26],

magnetocaloric effect [27, 28], negative thermal expansion [29], and nearly zero temperature coefficient of resistivity [30, 31] have been found. Especially, the thermoelectric properties of ternary compounds crystallizing in APV structures with narrow band gaps and dense electronic states near the Fermi level have been extensively investigated [32]. For example, the coexistence of lightweight and triply degenerate conduction band pockets in Rb_3AuO results in a high power factor reaching 5.5 mW/mK^2 at 800 K [33]. For Ba_3GeO, high valley degeneracy greatly improves the ZT from 0.4 to 1.1 when the $Pm\bar{3}m$ phase is distorted into the $Pnma$ phase [34]. Recently, high-throughput (HTP) DFT screening has been used to accelerate the exploration of more stable APVs [1, 2]. In our prior HTP-DFT analysis, we identified magnesium-based nitride antiperovskite materials (Mg_3XN; where X = P, As, Sb, Bi) as stable compounds. Moreover, the Mg_3XN has been employed in higher efficient tandem solar cells as they generate high levels of power while remaining stable [35]. In particular, Mg_3PN has a relatively high absorption coefficient, photoconductivity, and extinction coefficient deriving from its wide direct band gap nature [36]. The Mg_3SbN films are expected to be a promising photovoltaic solar cell absorber due to the large dielectric constant and low hole-effective mass [37].

However, comprehensive investigations on the thermal and electronic transport properties of magnesium-based APV compounds have been lacking, particularly due to the challenge posed by the existence of imaginary phonon frequencies. This issue has impeded the conventional solution of the BTE from accurately determining thermal conductivity in these structures. Additionally, the conventional first-principles theory of thermal conductivity based on the lowest-order perturbation treatment frequently results in the lattice thermal conductivity exhibiting the T^{-1} dependence [38, 39], which mainly stems from the following reason: (i) temperature-independent interatomic force constants (IFCs) [40, 41] and (ii) the activation of all phonon modes and the adherence to the Bose-Einstein distribution occur above the Debye temperature [42]. Such an approach, however, is inadequate to describe the temperature-responsive κ_L for strongly anharmonic materials, as they are affected by phase space renormalization, four-phonon scattering, and off-diagonal terms of heat flux operators [43–45]. For example, strong anharmonicity caused by locally asymmetric vibrations in Mg_3Sb_2 leads to a weaker temperature dependence as of $T^{-0.48}$ [46]. Therefore, correctly processing the temperature-responsive κ_L by anharmonic renormalization is of great significance for the accurate calculation of thermoelectric performance.

In this work, we perform a detailed stability analysis of APV Mg_3XN with the $Pm\bar{3}m$ phase, including the thermodynamic, thermal, mechanical, and dynamical stabilities. Meanwhile, we investigate the correlative thermal and electronic transport properties, as well as the thermoelectric performance, to evaluate their prospects for thermoelectric applications. The calculations have been conducted using the self-consistent phonon (SCP) theory, incorporating four-phonon (4ph) scattering, electron-phonon (e-ph) coupling, and the Boltzmann transport equation (BTE). This process adhered to the procedural flow depicted in Figure 1. Our results demonstrated that the presence of potential high-order anharmonicity in Mg_3PN and Mg_3AsN, induced by lattice distortion, affects not only the renormalization of vibrational eigenvalues but also the correction of the imaginary part of phonon self-energy. Simultaneously, atypical temperature-responsive lattice thermal conductivity (κ_L) caused by the renormalization of phonons significantly influences their overall thermoelectric performance, especially at elevated temperatures. Ultimately, Mg_3BiN exhibits the highest ZT values, measuring at 1.03 and 1.01 for n-type and p-type doping at 900K, respectively, underscoring its potential in the realm of thermoelectric applications. Our study highlights the significance of atypical temperature-responsive k_L in influencing thermoelectric performance, challenging conventional three-phonon diagram in the field of thermoelectric materials.

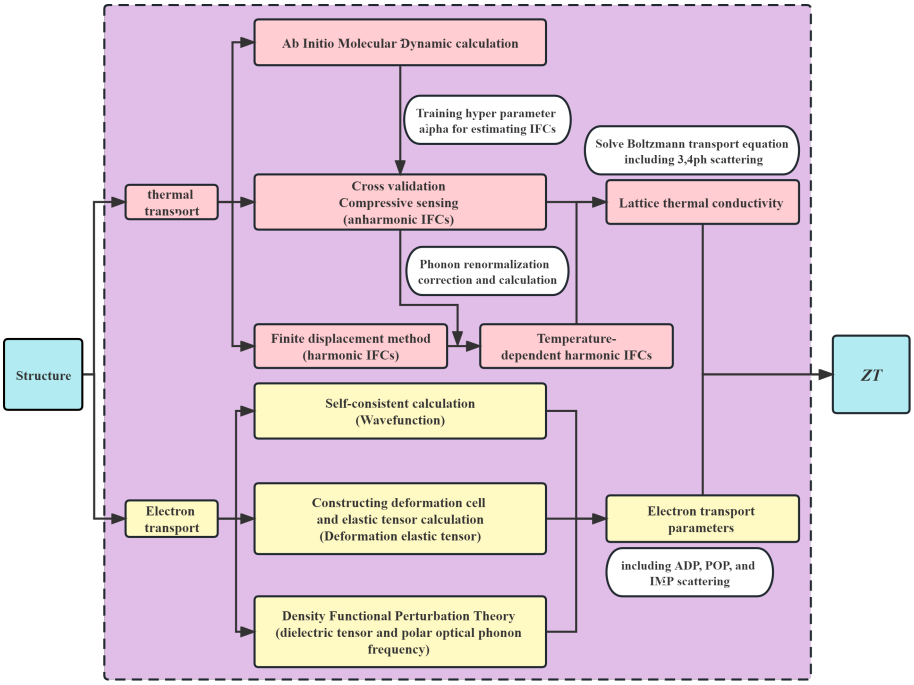

Figure 1: Workflow of the thermoelectric property calculations.

2. Methods

We performed all the calculations using the Vienna ab initio simulation package (VASP) code [47], which employs the projector augmented wave (PAW) method [48] and a plane wave basis set. The Perdew–Burke–Ernzerhof exchange-correlation functional revised for solids (PBEsol) [49] was employed. The convex hull is constructed with reference to the open quantum materials database (OQMD). [50]. The compressive sensing lattice dynamics (CSLD) technique was employed to obtain the anharmonic force constants [51], and we have captured the temperature-responsive anharmonic phonon energy by combining it with the self-consistent phonon (SCP) theory, as implemented in the ALAMODE code [52]. The FourPhonon package has been utilized to iteratively solve the linearized phonon Boltzmann transport to evaluate the lattice thermal conductivity [53, 54]. The thermoelectric properties, including carrier mobility (μ), Seebeck coefficient (S), electrical conductivity (σ), and electronic thermal conductivity (κ_e) were computed using the AMSET code with the adjusted band gap from HSE06 and spin–orbit coupling (SOC) included [55]. The net atomic charges and the overlap populations was obatined based on the density-derived electrostatic and chemical (DDEC6) method in CHARGEMOL [56–58]. More details of the computational processes are presented in the supporting information.

3. Results and Discussion

3.1. Structures and Stability Evaluation

3.1.1. Crystal Structures

Antiperovskite (APV) can be seen as a charge-reversal structure of perovskite, where positive and negative charges occupy opposite positions. In comparison to traditional perovskites, the general formula for the APV structure with the cubic space group $Pm\overline{3}m$ can be expressed as $A_3^{z+}X^{m-}B^{n-}$, where A represents cation, and X and B are anions of different sizes, as depicted in Figure 2. The octahedral sites are occupied by cations instead of anions, endowing the APVs with unusual physical and chemical characteristics associated with d-spin state/band structure or ionic peculiarity [59]. For magnesium-based APV Mg_3XN (X = P, As, Sb, Bi), the Mg, X, and N atoms are located at positions A, X, and B, respectively. Each N anion occupies the central position of an octahedron formed by six Mg cations, while each X anion is surrounded by twelve Mg cations in a pseudo-cage

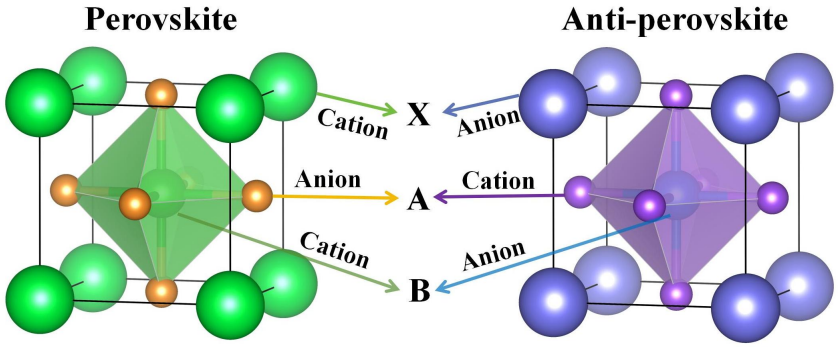

Figure 2: Structure comparison of ideal perovskite and antiperovskite with the cubic space group $Pm\bar{3}m$.

arrangement. The calculated equilibrium lattice parameters are 4.178 Å for Mg_3PN, 4.231 Å for Mg_3AsN, 4.374 Å for Mg_3SbN, and 4.430 Å for Mg_3BiN, receptively. Apparently, the lattice parameters of these compounds increase with the increase of the X-atom radius. In addition, the difference in lattice parameters between our study and other work is within a reasonable margin of error, as listed in Table 1.

Table 1: The lattice parameters and volume of primitive cell comparison with results of previous work.

APVs	$a = b = c$ (Å)	V (Å^3)	Reference
Mg_3PN	4.178	72.9	This work
	4.183	73.19	Ref [60]
	4.153	71.62	Ref [61]
Mg_3AsN	4.231	75.7	This work
	4.239	76.1	Ref [60]
	4.217	74.9	Ref [62]
Mg_3SbN	4.374	82.6	This work
	4.377	83.8	Ref [60]
	4.351	82.3	Ref [62]
Mg_3BiN	4.430	86.9	This work
	4.441	87.5	Ref [60]
	4.397	85.0	Ref [61]

3.1.2. Thermodynamical and Thermal Stability

The formation energy (E_f = E_{Mg_3XN} - ($3E_{Mg}$ + E_X + E_N)) and the convex hull distance ($\Delta E_H = E_f(Mg_3XN)$ - E_f(competing phases)) are two important criteria for determining the thermodynamic stability [63]. Firstly, the calculated E_f is -0.807 eV/atom for Mg_3PN, -0.768 eV/atom for Mg_3AsN, -0.650 eV/atom for Mg_3SbN, and -0.501 eV/atom for Mg_3BiN, respectively. Secondly, the ternary phase diagrams of four APVs have been further constructed to measure the convex hull distance by considering all the competing phases (Figure S1, Supporting Information). Among them, the Mg_3SbN and Mg_3BiN are located on the convex hull ($\Delta E_H = 0$). While the ΔE_H of Mg_3PN and Mg_3AsN are 23 and 5 meV per atom which is within the acceptable range for convex hull, respectively, they are deemed as metastable. As a result, all these APV compounds are expected to be synthesized experimentally under appropriate conditions. Excitingly, the Mg_3AsN and Mg_3SbN with cubic phase have been successfully prepared by the reaction of pnictogen and Mg_3N_2 at 800°C [62]. Additionally, the performance of APVs under extreme temperature conditions also depends on their thermal stability. The thermal stability was tested by performing ab initio molecular dynamics (AIMD) simulations with 30 ps at 300, 600, and 900 K [64]. The total energy of Mg_3XN fluctuates in a narrow range with time evolution for all cases (Figure S2, Supporting Information). As a result, these materials can still maintain their initial crystal state at very high temperatures, which enhances their application value.

3.1.3. Mechanical Stability

Generally, the crystal will undergo certain deformation when it is subjected to mechanical stress, and this deformation will lead to the reduction of the energy. If the energy reduction exceeds a critical threshold, the structure becomes unstable and undergoes failure modes such as buckling or fracture. Therefore, mechanical stability analysis is a method to evaluate whether a structure can maintain stability under stress. The mechanical stability can be expressed by the strain energy (W), which is derived from the difference in energy between the strained (E_{str}) and unstrained (E_{unstr}) states according to the elastic constants [65, 66].

$$W = E_{str} - E_{unstr} = \frac{1}{2}\sum_{i,j} C_{i,j}\epsilon_i\epsilon_j \quad (1)$$

Table 2: The calculated elastic constants C_{ij} (GPa), Bulk modulus B (GPa), Shear Modulus G (GPa), Poisson's Ratio (ν), Pugh's Ratio (B/G), Young's Modulus E (GPa), and average acoustic phonon group rate v_a (m/s).

APVs	C_{11}	C_{12}	C_{44}	B	G	ν	B/G	E	v_a
Mg_3PN	185.8	42.8	78.9	90.5	75.9	0.17	1.19	178	5853
Mg_3AsN	170.4	44	76.3	86	71	0.18	1.22	167	4919
Mg_3SbN	138.2	46.6	69.9	77.1	59.9	0.19	1.31	141	4165
Mg_3BiN	123.2	45.2	63.7	71.2	53.8	0.20	1.36	126	3361

where $C_{i,j}$ and ϵ represent second-order elastic tensors and strain, respectively. For cubic APVs, there are three independent elastic constants: C_{11}, C_{12}, and C_{44}. Table 2 lists all elastic constants C_{ij}, in which all C_{ij} satisfy correlative mechanical stability criteria ($C_{11}-C_{12}>0, C_{11}+2C_{12}>0, C_{44}>0$), confirming they are mechanically stable [66].

Meanwhile, various mechanical properties parameters, including bulk modulus B, shear modulus G, Pugh's ratio (B/G), and Young's modulus E are also discussed. Clearly, there is a negative correlation between the atomic number of the X atom and the values of B and G, which is in line with previous research [67]. The upper limit of the B and G for four APVs occurs in Mg_3PN with 90.5 and 75.9 GPa, respectively. This indicates that the Mg_3PN resists deformation the most and potentially has a high degree of compressibility. By contrast, the B and G values of Mg_3BiN are the smallest, which are 71.2 GPa and 53.8 GPa, respectively. Simultaneously, all Mg_3XN compounds exhibit brittle because the values of B/G are less than 1.75 according to the Pugh criterion [68]. Moreover, the larger the E, the more significant the stiffness trend of the material. Thus, Mg_3PN (178 GPa) and Mg_3BiN (126 GPa) are the materials with the highest and lowest hardness, respectively.

In fact, the average phonon rates (v_a) associated with the acoustic branch can be quantitatively analyzed by monitoring the elastic modulus near the center of the Brillouin region, which is often regarded as an important indicator for assessing the thermal transport characteristics, as follow [69]

$$v_a = (\frac{1}{3})^{-\frac{1}{3}} \left\{ 2(\frac{G}{\rho})^{-\frac{3}{2}} + (\frac{B+\frac{4}{3}G}{\rho})^{-\frac{3}{2}} \right\}^{-\frac{1}{3}} \quad (2)$$

Generally, crystals with low bulk and shear modulus possess "soft bonding" properties [70]. As a result, the average acoustic phonon group rate

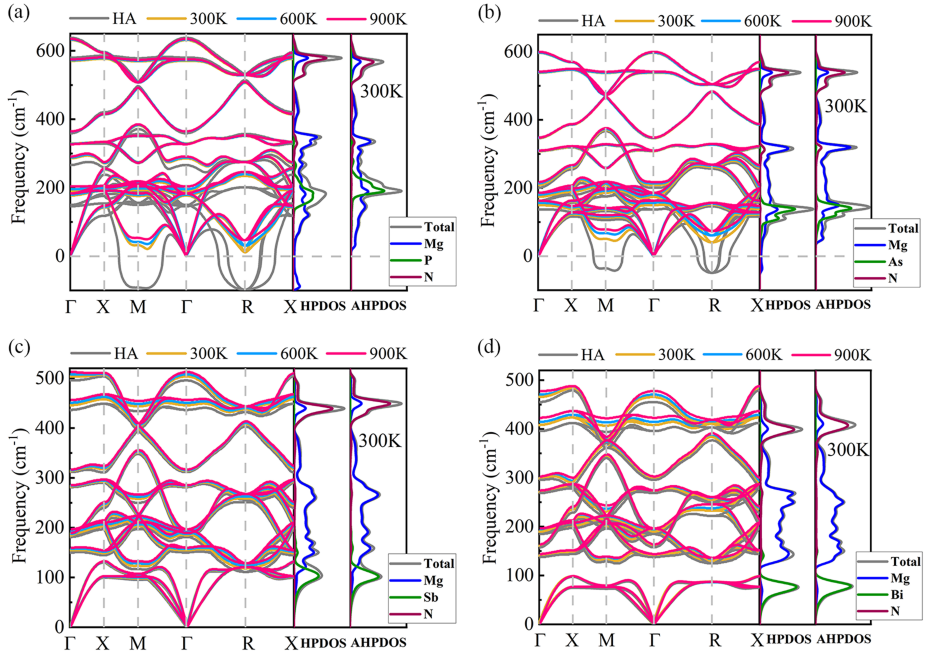

Figure 3: The calculated phonon dispersions and corresponding phonon density of states (PDOS) at different temperatures for (a) Mg_3PN, (b) Mg_3AsN, (c) Mg_3SbN, and (d) Mg_3BiN, where the result of HA represents the 0 K.

v_a decreases successively due to the reduction of bulk and shear modulus from Mg_3PN to Mg_3BiN, which are conducive to limiting the transport of heat-carrying phonons.

3.2. Phonon dispersion

Turning now to the lattice dynamics of Mg_3XN. The phonon dispersion curves obtained within the harmonic approximation are shown in Figure 3. Two imaginary phonon modes which transform as irreducible representations (irreps) M_2^+ and R_5^- are found at the special points for Mg_3PN and Mg_3AsN, while the Mg_3SbN and Mg_3BiN are dynamically stable at 0 K. In particular, we observed that the vibration of Mg atoms mainly contributes to the imaginary frequency patterns in Mg_3PN and Mg_3AsN. Indeed, the Mg atoms exhibit larger mean squared atomic displacements (MSDs) along with z-direction (Figure S3, Supporting Information). After visualization analysis, the softening modes at points M and R in Mg_3PN and Mg_3AsN

are related to in-phase and out-of-phase tilting of Mg_6N octahedral units, respectively, as shown in Figure 4. To gain a deeper insight, we calculated the frozen phonon potential energy surface (PES) as a function of normal mode coordinates Q at the M and R points. It is worth noting that both soft modes at the M and R points of Mg_3PN and Mg_3AsN prove lattice or dynamical instability as the presence of double-well potential, where the minimum energy is not at the zero-tilt amplitude ($Q_1 = Q_2 = 0$) but outside it [71]. The imaginary phonon modes of the Mg_3PN and Mg_3AsN are significantly hardened after the anharmonic renormalization, including the loop diagram ascribing from the quartic anharmonicity at elevated temperatures, while the corresponding high-frequency optical modes are hardly affected. On the contrary, the phonon self-energy correction of the Mg_3SbN and Mg_3BiN is mainly reflected in the medium and high-frequency optical phonons. The above analysis demonstrates that accurate treatment of anharmonic interactions is extremely important for lattice dynamics modeling.

The Goldschmidt tolerance factor τ was discussed to further explain the lattice dynamic stability of APV [72, 73], which is defined by $\tau = (r_X + r_{Mg})/[\sqrt{2}(r_N + r_{Mg})]$, where r_{Mg}, r_N, and r_X represent the radii of Mg^{3+} cation, N^{3-} anion and X^{3-} anion, respectively. The relatively small τ of Mg_3PN (0.85) and Mg_3AsN (0.87) can serve as evidence for lattice distortion, hinting at the presence of potential strong anharmonicity. While the τ of Mg_3SbN (0.95) and Mg_3BiN (0.97) indicates that the two anions have ideal sizes, thus ensuring the cubic configuration. On the contrary, the loop diagram correction of the Mg_3SbN and Mg_3BiN is mainly reflected in the medium and high-frequency optical phonons. Furthermore, the imaginary harmonic frequency of Mg_3PN and Mg_3AsN means the occurrence of the phase transition at low temperatures and the phase transition temperature can be reasonably estimated by the equation [74]

$$\Omega_q^2(T) = a(T - T_c) \tag{3}$$

It is worth noting that the frequency shift associated with the bubble self-energy is also taken into account to improve quantitative consistency. This has been proved to be of great significant for the accurate estimation of the theoretical phase transition temperature in halide perovskite $CsPbBr_3$ [75]. Considering that the soft-mode minimum energy occurs at R, it indicates that the out-of-phase tilting plays a dominant role in the phase transition. Based on the lowest phonon mode at R point of Mg_3PN and Mg_3AsN, the

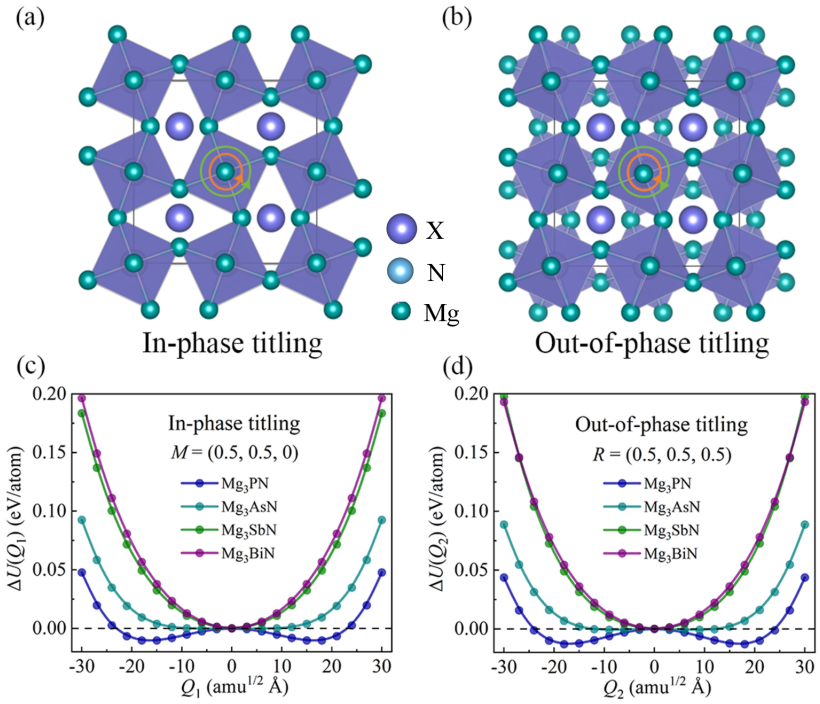

Figure 4: Crystal structure of Mg_3XN with displacement pattern of the soft mode at the (a) M and (b) R point, wherein the orange and green circles with arrows are depicted for the displacements of the in-phase and out-of-phase tilting displacement of Mg_6N units, respectively. Frozen phonon potential energy surface (PES) of lowest phonon mode at (c) M and (d) R point as a function of normal mode coordinates Q. The circles represent the results of the DFT calculation, and the solid lines represent the quartic fit of the energy.

corresponding critical temperature T_c of Mg_3PN and Mg_3AsN are 167 K and 56 K, respectively.

3.3. Lattice thermal transport

3.3.1. Lattice thermal conductivity with 3ph scattering

The lattice thermal conductivities κ_L^{3ph} of Mg_3XN, including only three-phonon interaction in the temperature range from 300 to 900 K, are described in Figure 5. Obviously, κ_L^{3ph} is 5.5 W/mK for Mg_3PN, 6.4 W/mK for Mg_3AsN, 7.9 W/mK for Mg_3SbN, and 5.6 W/mK for Mg_3BiN at 300 K, respectively. Additionally, the coherence contribution κ_c described by the off-diagonal terms of the heat flux operators was also evaluated in our

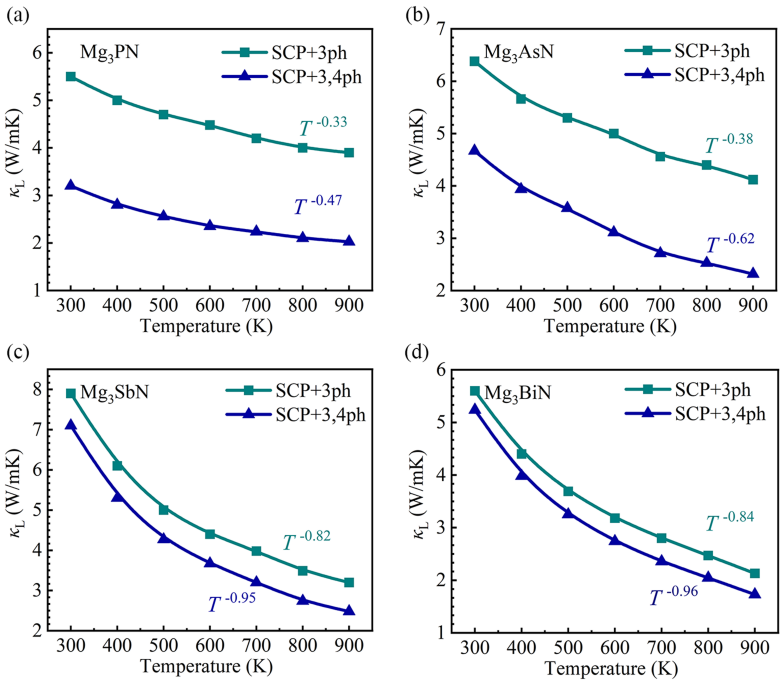

Figure 5: The calculated temperature-responsive κ_L of (a) Mg_3PN, (b) Mg_3AsN, (c) Mg_3SbN, and (d) Mg_3BiN from 300 to 900 K by using SCP+3ph and SCP+3,4ph, respectively.

calculations, which represents the wave-like tunneling transport channels. Especially, it is only when the phonon mean free path (MFP) approaches the atomic spacing that the non-diagonal contribution becomes non-negligible [71, 76]. The results show that the κ_c of Mg_3XN is almost negligible compared to propagation contribution (Figure S4, Supporting Information).

3.3.2. Microscopic mechanism of thermal conductivity

The microscopic mechanism of different κ_L^{3ph} among Mg_3XN compounds can be understood based on detailed analysis. Following BTE, thermal conductivity mainly involves three variables, i.e., $\kappa_L = \frac{1}{VN_0}\sum C_V v_g^2 \tau_q$, where the V, N_0, C_V, v_g, and τ_q represent the unit-cell volume, sampling number, specific heat, phonon group velocity, and lifetime, respectively. The lattice-specific heat C_V gradually declines with the increasing atomic number of the nitrogen group element X at the same temperature because the range of phonon distribution $n(\omega)$ narrows [77] (Figure S5, Supporting Information).

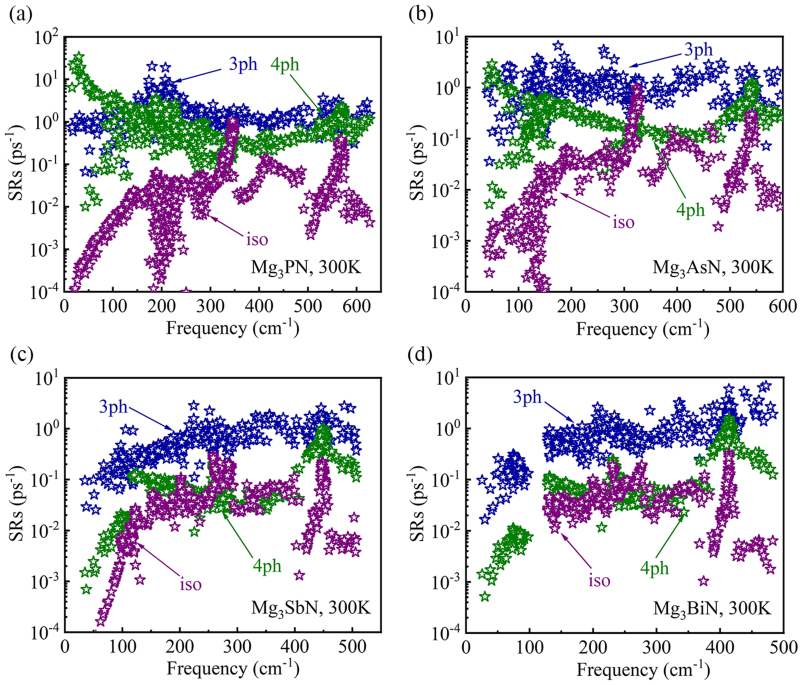

Figure 6: Three-phonon (3ph), four-phonon (4ph), and isotope scattering rates of (a) Mg_3PN, (b) Mg_3AsN, (c) Mg_3SbN and (d) Mg_3BiN at 300 K.

Meanwhile, the phonon group velocity v_g decreases evidently because the phonon frequencies ω_{ph} soften, which confirms the previous analysis based on the bulk and shear modulus for predicting the phonon rates. (Figure S6, Supporting Information). However, observing only these two parameters does not explain the trend of thermal conductivity in Mg_3XN.

The phonon lifetime τ_q, which is inversely proportional to the phonon scattering rate, plays an important role in determining κ_L. The scattering rate is usually regarded as positively correlated with the Grüneisen parameter γ, which is proportional to the cubic anharmonicity. Surprisingly, Mg_3PN and Mg_3AsN exhibit a larger γ, which is consistent with previously mentioned lattice distortions (Figure S7, Supporting Information). We find that the cubic anharmonicity decreases with the increase of the radius of X^{3-} anion. Therefore, compared with Mg_3AsN and Mg_3SbN, Mg_3PN has a lower κ_L^{3ph} which can be ascribed to its strongest cubic anharmonicity. Nevertheless, this trend seems to be broken by Mg_3BiN as its κ_L^{3ph} is comparable to Mg_3PN.

After careful investigation, the puzzling abnormal change derives from special rattle-dominated vibrational modes in Mg_3BiN [78–80]. Relative flattening of the acoustic modes can limit the scattering process to specific channels that conserve the momentum and energy simultaneously, thereby widening the phase space W_{3ph} [81]. Specifically, for any mode q_0 ($\omega_0 > \omega_{flat}$), the scattering channel is greatly restricted to two specific modes (q_1, ω_0-ω_{flat}) and (q_0-q_1, ω_{flat}) to ensure conservation, and reaches a maximum at $\omega_0 = 2\omega_{flat}$. (Figure S8, Supporting Information)

3.3.3. Corrected imaginary part of phonon self-energy - 4ph scattering

However, it should be noted that κ_L^{3ph} based on renormalization is only relying on the quartic anharmonicity correction to the real part of the phonon self-energy, while its correction to the imaginary part needs to consider four-phonon (4ph) scattering [82, 83]. Refining the SCP+3,4ph model by further introducing 4ph scattering processes into the improved model, the predicted $\kappa_L^{3,4ph}$ are 3.2 W/mK for Mg_3PN, 4.6 W/mK for Mg_3AsN, 7.1 W/mK for Mg_3SbN, and 5.3 W/mK for Mg_3BiN at 300 K, respectively, decreased by 42%, 27%, 10%, and 6% in comparison to κ_L^{3ph}, respectively. Noticeably, the quartic anharmonicity of Mg_3PN and Mg_3AsN embodies not only fluctuations in phonon frequencies but also the four-phonon scattering rates, as shown in Figure 6. The 4ph scattering rates of Mg_3PN are roughly as high as those of the 3ph processes at 300 K but are dominant at low frequency. In the upper left part of Figure 6(a), a distinctive feature with scattering rates decreasing with increasing frequency is observed in 4ph scattering processes of Mg_3PN when the frequency less than 100 cm^{-1}, which can be attributed to the presence of the Mg-dominated soft modes. Such a similar feature was also reported for lead-free halide double perovskites $Cs_2AgBiBr_6$ [84]. Whereas the 4ph scattering rates for Mg_3SbN and Mg_3BiN are only comparable to the isotope scattering.

Furthermore, we also check the scattering rates of each sub-process of 4ph interactions, and it is found that the redistribution processes ($\lambda + \lambda' \rightarrow \lambda'' + \lambda'''$) dominate the 4ph scattering processes for all four APVs, as the simplicity of satisfying the selection rule [85] (Figure S9, Supporting Information). At last, the 4ph scattering can be divided into normal and Umklapp processes, where the former redistributes momentum between phonons and the latter impedes phonon transmission. Predominantly, the Umklapp process governs the 4ph scattering, which indicates that thermal resistance serves as the chief cause of the κ_L reduction (Figure S10, Supporting Information).

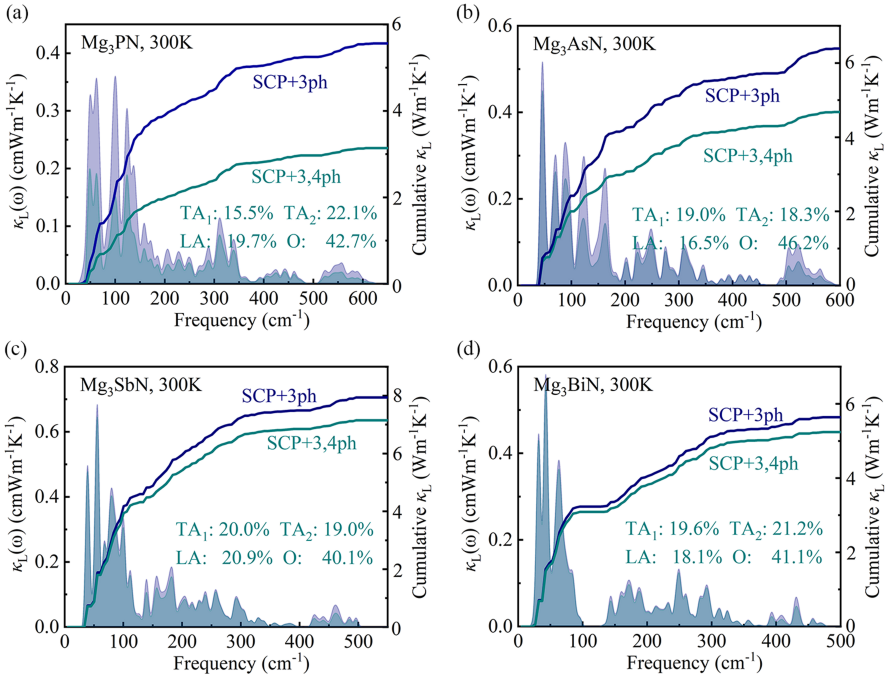

Figure 7: The spectral/cumulative phonon thermal conductivity of (a) Mg_3PN, (b) Mg_3AsN, (c) Mg_3SbN, and (d) Mg_3BiN at 300 K.

3.3.4. Atypical temperature-responsiveness and modal contribution

It is usually known that the temperature responsiveness of κ_L conforms $\kappa_L \sim T^{-1}$ in common semiconductors. Yet, abnormally weak temperature responsiveness is observed in Mg_3PN and Mg_3AsN. For example, the temperature responsiveness of κ_L^{3ph} is reduced to $T^{-0.33}$ and $T^{-0.38}$ for Mg_3PN and Mg_3AsN, respectively. The addition of 4ph scatterings can only enhance the relationship to $T^{-0.47}$ and $T^{-0.62}$, respectively. Such weak temperature responsiveness is also seen in other perovskites with strong anharmonicity, such as oxide perovskite $BaTiO_3$ ($T^{-0.49}$), and fluoride perovskite $CsSrF_3$ ($T^{-0.61}$), $RbCdF_3$ ($T^{-0.57}$), $CsHgF_3$ ($T^{-0.67}$) [86]. This further highlights the necessity of anharmonic renormalization in calculating κ_L by considering 4ph scatterings. In contrast to Mg_3PN and Mg_3AsN, the temperature responsiveness is confirmed in Mg_3SbN and Mg_3BiN, i.e., $\kappa_L^{3ph} \sim T^{-0.82}$ and $T^{-0.84}$ for Mg_3SbN and Mg_3BiN, respectively; with $\kappa_L^{3,4ph} \sim T^{-0.95}$ and $T^{-0.96}$, respectively. Interestingly, the $\kappa_L^{3,4ph}$ of Mg_3BiN (1.72 W/mK) becomes even

lower than that of Mg_3PN (2.12 W/mK) at 900 K, due to the enhanced temperature responsiveness for the thermal conductivity in Mg_3BiN. In this regard, the atypical temperature-responsive lattice thermal conductivity can have a strong influence on the thermoelectric properties of the material, as discussed later.

The spectral/cumulative thermal conductivity as a function of frequency is displayed to illustrate the effect of different modes in Figure 7. It is clear that the acoustic and medium-frequency optical modes contribute significantly to the κ_L in comparison to the high-frequency optical modes because the low group velocity caused by relatively flat phonon dispersion restricts the transport capacity of the latter. Also, the high-frequency optical phonons are largely not thermally excited at low temperatures according to the Bose-Einstein distribution. Simultaneously, the thermal conductivity of Mg_3PN and Mg_3AsN is mainly suppressed in the low-frequency region, driven by the remarkable 4ph scattering below 200 cm^{-1}. Moreover, the κ_L of Mg_3XN is expected to be further restricted through nanoengineering considering the maximum MFP [87]. For instance, the $\kappa_L^{3,4ph}$ of Mg_3BiN will be reduced from 5.24 to 2.6 W/mK when the MFP is limited to 10 nm (Figure S11, Supporting Information).

3.4. Electronic structures

Figure 8 displays the band structures and the corresponding partial densities of states (pDOS) of Mg_3XN. The band gaps of Mg_3XN exhibit positive linear correlations with the inverse lattice constants. Among them, the Mg_3PN (with a gap of 2.47 eV) and Mg_3AsN (with a gap of 2.15 eV) exhibit direct band gaps at the Γ point, while Mg_3SbN (with a gap of 1.23 eV) and Mg_3BiN (with a gap of 0.73 eV) have the valence band maximum (VBM) at the Γ point and the conduction band minimum (CBM) at the M point. According to the pDOS, the valence bands of Mg_3XN are predominantly composed of the p states, i.e., the overlap of $Mg[3p]$ - $N[2p]$ and $Mg[3p]$ - $X[p]$ states. The strong p-p hybridization also accounts for the wide valence band width of Mg_3XN of about 6 eV (Figure S12, Supporting Information).

The crystal orbital Hamilton population (COHP) is evaluated to explore the bonding nature (Figure S13, Supporting Information). Closing to the Fermi level, the N-X and Mg-N present anti-bonding states, while the Mg-X shows bonding states. The net atomic charge and overlapping population can serve as effective indicators to qualitatively assess the bond type and

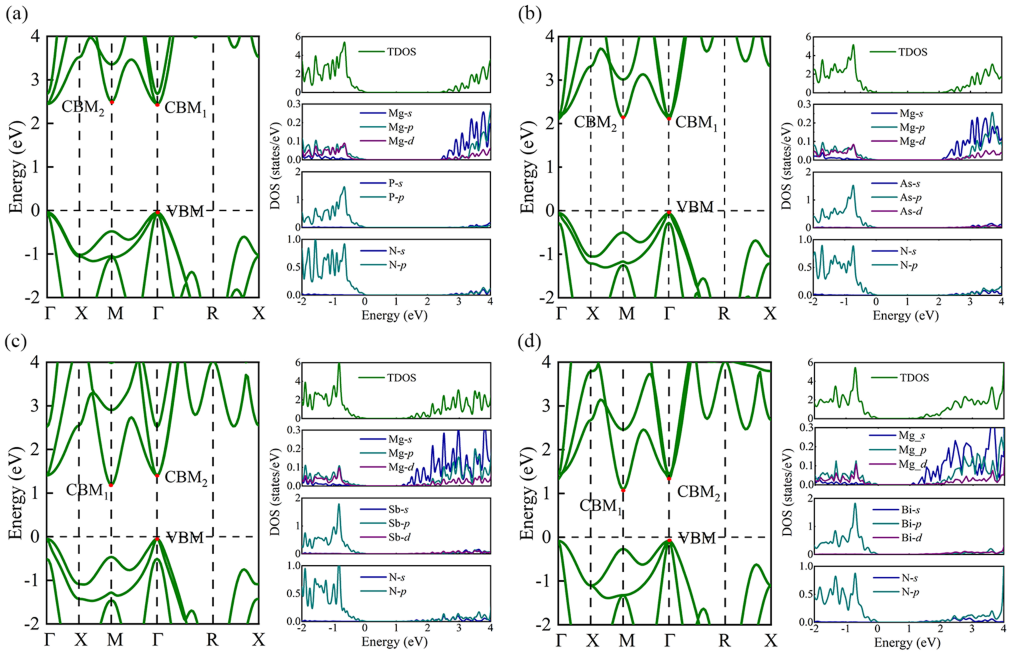

Figure 8: Electronic band structure and partial densities of states (pDOS) of (a) Mg_3PN, (b) Mg_3AsN, (c) Mg_3SbN, and (d) Mg_3BiN based on the HSE06+SOC.

quantitatively measure the bond strength, as demonstrated in Figure 9 and Table 3. As the electronegativity ascends from Bi to P, the charge transfer becomes more pronounced and the ionic character intensifies accordingly. In contrast, the extent of orbital overlap between atoms is reduced, implying a weaker covalent contribution to the bonding. The overall conductivity is likely to decrease with the increasing electronegativity of X, because the carrier dynamics are modulated by the distinct nature of ionic and covalent bonds. Specifically, the ionic bonding impedes the carrier motion by virtue of the larger charge transfer, while the covalent bonds enable the carrier transitions by the smaller charge difference and the wider orbital overlap, which facilitate the intrinsic excitation.

Furthermore, the s states of Mg have a negligible contribution to densities of states owing to the symmetry restriction imposed by the p states from X and N [88]. The conduction bands are dominated by the $Mg[3s]$ and $Mg[3p]$ states. It is noted that the symmetrically constrained chemical bonding nature of Mg_3XN renders the system more ionic than other nitrides based

Table 3: The transferred and shared charges (|e|) between atoms in Mg_3XN (X = P, As, Sb, Bi).

	Transferred charge (|e|)				Shared charge (|e|)		
APVs	Mg	X	N	Average	Mg-X	Mg-N	Average
Mg_3PN	1.264	-1.846	-1.947	1.517	0.125	0.298	0.160
Mg_3AsN	1.250	-1.830	-1.920	1.500	0.130	0.290	0.162
Mg_3SbN	1.225	-1.820	-1.854	1.470	0.143	0.269	0.167
Mg_3BiN	1.207	-1.793	-1.829	1.449	0.145	0.263	0.169

Table 4: The calculated band gaps E_g by using PBE+SOC and HSE06+SOC, Born effective charges Z^*, dielectric permittivity tensors ε_∞, and effective polar optical phonon frequency ω_{po}.

APVs	E_{PBE}	E_{HSE}	ε_∞	${Z_{Mg}}^*{}_{\parallel}$	${Z_{Mg}}^*{}_{\perp}$	${Z_X}^*$	${Z_N}^*$	ω_{po}
Mg_3PN	1.74	2.48	9.121	2.625	1.675	-3.502	-3.424	8.97
Mg_3AsN	1.30	2.15	10.318	2.699	1.666	-3.481	-3.584	8.85
Mg_3SbN	0.56	1.23	12.787	2.768	1.751	-3.645	-3.642	8.56
Mg_3BiN	0.19	0.73	15.649	2.913	1.721	-3.615	-3.931	8.20

on the classic metallic–ionic–covalent axes of van Arkel triangles [89], as seen in Ref [90] (Figure S14, Supporting Information).

3.5. Electronic transport

The coexistence of high-dispersion band edges and electronic band degeneracy of Mg_3XN gives rise to compelling transport properties. For instance, the degeneracy of light and heavy bands for four APVs occurs at the Γ point, with the former favoring a high electronic conductivity and the latter providing a larger Seebeck coefficient [92]. After considering the acoustic deformation potential (ADP), polar optical phonon (POP), and ionized impurity (IMP) scattering, the precise carrier relaxation time can be obtained. As shown in Figure 10, the electronic conductivity σ of Mg_3XN increases sequentially from Mg_3PN to Mg_3BiN, which is consistent with the trend of their carrier mobility μ (Figure S15, Supporting Information). There are two main reasons to explain the discrepancy of their carrier mobility: (i) the negatively correlated dielectric tensor causes the dominant POP scattering to weaken sequentially (Table 4 and Figure S16, Supporting Information). (ii) the positively correlated high-dispersion band edges lead to smaller carrier

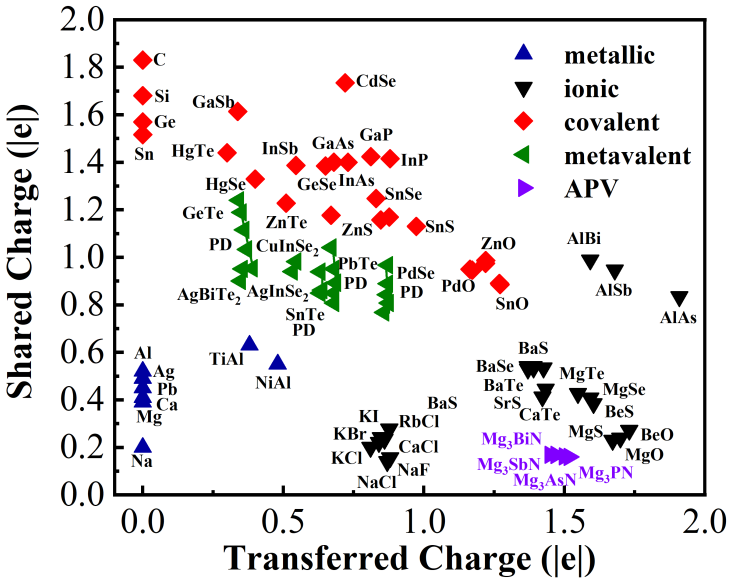

Figure 9: Charge sharing and charge transfer map including metallic, ionic, covalent, and metavalent bonding. Symbols labeled "PD" represent the Peierls distorted structures of the same compound. Note: The rest of the data in this chart is from Ref [91]

effective masses, as listed in Table 5. Concurrently, the electrical conductivity σ is inversely proportional to temperature T, which is attributed to the increased scattering rates dominated by the electron-phonon interaction. Emphatically, the positive phonon frequency shifts induced by the quartic anharmonicity will reduce the electron-phonon coupling (EPC) strength because the electrons at the band edge are more susceptible to scattering by low-lying phonons, ultimately improving the carrier mobility and electrical conductivity [93, 94]. Hence, our calculations are based on a relatively conservative situation. Additionally, considering that the electrical thermal conductivity κ_e follows the Wiedemann-Franz law ($\kappa_e = L\sigma T$) [95], where L is the Lorenz number. Therefore, it exhibits similar changes with electrical conductivity σ (Figure S17, Supporting Information).

The Seebeck coefficient $|S|$ appears to have an opposite trend as the electronic conductivity σ. For instance, the Seebeck coefficient $|S|$ is proportional to the carrier effective mass, which follows the ordering $Mg_3PN > Mg_3AsN >$

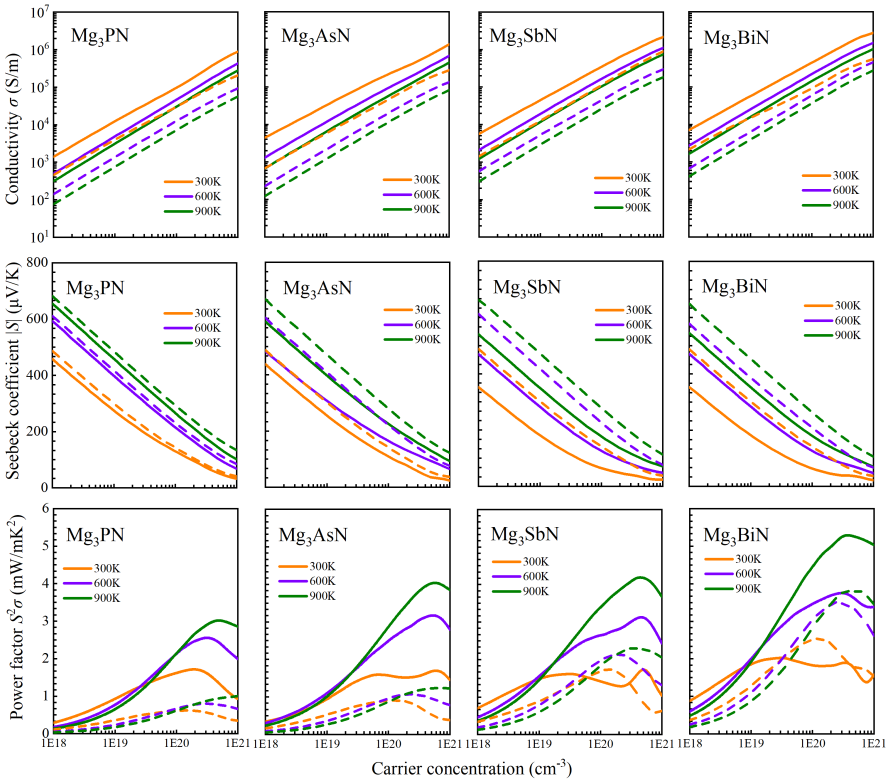

Figure 10: The electronic transport parameters electrical conductivity σ, Seebeck coefficient $|S|$, and power factor PF of Mg_3XN at 300, 600, and 900 K. The solid and dashed lines correspond to n-type and p-type systems, respectively.

Table 5: The effective masses of holes (m_h^*) and electrons (m_e^*) for the M_3XN, which are calculated using the HSE06 functional with spin-orbit coupling.

APVs	VBM-CBM	Γ-M		Γ-R	
		m_h^*	m_e^*	m_h^*	m_e^*
Mg_3PN	Γ-Γ	0.672	0.441	0.540	0.312
Mg_3AsN	Γ-Γ	0.584	0.391	0.490	0.254
		Γ-M	M-Γ	Γ-R	M-X
		m_h^*	m_e^*	m_h^*	m_h^*
Mg_3SbN	Γ-M	0.390	0.194	0.310	0.194
Mg_3BiN	Γ-M	0.262	0.181	0.195	0.181

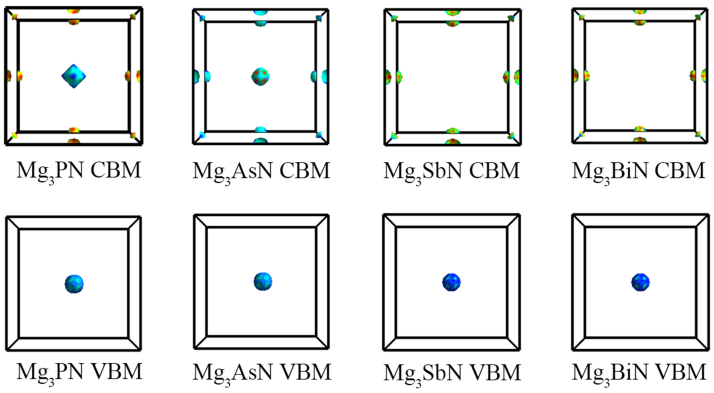

Figure 11: Energy isosurfaces of Mg_3XN at 0.1 eV above CBM and below VBM.

$Mg_3SbN > Mg_3BiN$. To elucidate the relationship, the energy isosurfaces of Mg_3XN are displayed in Figure 11. For CBM, two types of valley pockets in Mg_3PN and Mg_3AsN are located at the Γ and M points, respectively, which is consistent with the band structure. The negligible energy gap between CBM_1 and CBM_2 facilitates the participation of the secondary conduction band, thereby enhancing spatial degeneracy and the Seebeck coefficient. In contrast, the valley pockets of Mg_3SbN and Mg_3BiN appear only at the Brillouin zone boundary. For VBM, the valley pockets of the four APVs all emerge at the Γ point, but their energy pocket volume differs slightly as a result of the variation in the effective mass of the carriers. Moreover, the p-type systems have higher Seebeck coefficients than the n-type systems because of the presence of more electron-occupied states near VBM. In the condition of competing electronic transport parameters, the highest power factor PF is finally captured in Mg_3BiN, which means the maximum power output at the same temperature difference.

To this end, the ZT values of Mg_3XN are obtained at different temperatures and carrier concentrations, as illustrated in Figure 12. At room temperature, the n-type Mg_3PN shows the most excellent thermoelectric properties, with $ZT \sim 0.15$ due to its low lattice thermal conductivity. However, the temperature responsiveness of κ_L in Mg_3PN has been significantly weakened due to strong quartic anharmonicity with the increase of temperature, affecting its overall thermoelectric performance. At elevated temperatures, the optimal ZT is found in Mg_3BiN with 1.03 and 1.01 for n-type and p-

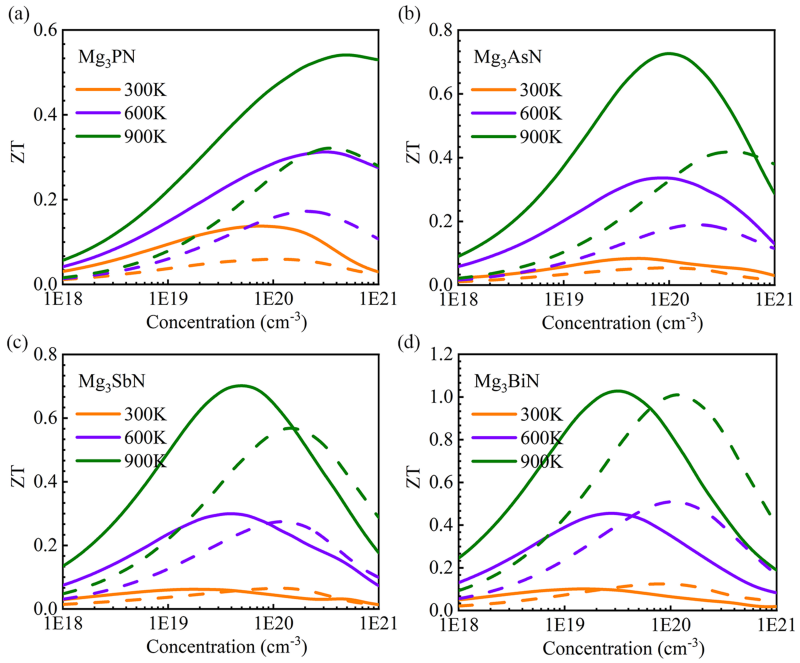

Figure 12: The thermoelectric figure of merit ZT as a function of carrier doping concentration of (a) Mg_3PN, (b) Mg_3AsN, (c) Mg_3SbN, and (d) Mg_3BiN at 300, 600, and 900 K.

type at 900K, respectively, which is attributed to the combination of the highest power factor PF and lowest κ_L caused by the temperature responsiveness with $T^{-0.96}$. Meanwhile, the optimum concentration for Mg_3BiN is far smaller compared to others, meaning it is easier to achieve the best thermoelectric performance. Thanks to a cost-effective preparation scheme and superior thermoelectric performance, Mg_3BiN is expected to be a promising candidate for high-temperature thermoelectric applications.

4. Conclusions

In summary, we investigated the thermal-electrical transport properties and thermoelectric performance of magnesium-based antiperovskite (Mg_3XN; X = P, As, Sb, Bi) with the cubic antiperovskite phase based on the self-consistent phonon (SCP) theory, electron-phonon scattering, and the Boltzmann transport equation. Our results show that the strong quartic anharmonicity in Mg_3PN and Mg_3AsN is not only manifested in phonon self-energy renormalization but also weakens the temperature responsiveness of the lattice thermal conductivity, thereby influencing the overall thermoelectric performance. While the Mg_3BiN exhibits the lowest thermal conductivity at elevated temperatures by combining its unique rattle-dominated vibrational modes with the strong temperature-responsive relationship with $T^{-0.96}$. Simultaneously, the combination of highly dispersive band edges and electronic band degeneracy of Mg_3XN results in remarkable electronic conductivity and large Seebeck coefficient, respectively, and the optimal power factor PF is captured in Mg_3BiN. Eventually, the maximum ZT value has been achieved in Mg_3BiN with 1.03 and 1.01 for n-type and p-type at 900K, respectively. We not only demonstrate that magnesium-based antiperovskite Mg_3BiN can serve as a highly promising thermoelectric material but also emphasize that the atypical temperature-responsive lattice thermal conductivity induced by strong anharmonicity can severely affect the thermoelectric performance of the material, especially at high temperature. This work offers guidance for tailoring the thermoelectric properties of strongly anharmonic materials in the future.

5. Acknowledgment

J.C.Y. and Y.H.L. contributed equally to this work. This work was supported by the National Natural Science Foundation of China (No. 52072188), the Program for Science and Technology Innovation Team in Zhejiang (No. 2021R01004), the National Academic Infrastructure for Supercomputing in Sweden, the Swedish National Infrastructure for Computing (SNIC) (NO. 2022-06725, 2018-05973) at Sigma and Tetralith Clusters, and the Vienna Scientific Cluster (VSC) in Austria. CS and WR acknowledge the Lichtenberg high-performance supercomputer of TU Darmstadt for the computational resources. Thanks the NHR-Verein e.V.(www.nhr-verein.de) for supporting this work within the NHR Graduate School of National High Performance Computing (NHR).

References

[1] H. K. Singh, Z. Zhang, I. Opahle, D. Ohmer, Y. Yao, H. Zhang, High-throughput screening of magnetic antiperovskites, Chemistry of Materials 30 (20) (2018) 6983–6991.

[2] H. K. Singh, A. Sehrawat, C. Shen, I. Samathrakis, I. Opahle, H. Zhang, R. Xie, High-throughput screening of half-antiperovskites with a stacked kagome lattice, Acta Materialia 242 (2023) 118474.

[3] B. Qin, D. Wang, X. Liu, Y. Qin, J.-F. Dong, J. Luo, J.-W. Li, W. Liu, G. Tan, X. Tang, et al., Power generation and thermoelectric cooling enabled by momentum and energy multiband alignments, Science 373 (6554) (2021) 556–561.

[4] J. Mao, H. Zhu, Z. Ding, Z. Liu, G. A. Gamage, G. Chen, Z. Ren, High thermoelectric cooling performance of n-type Mg_3Bi_2-based materials, Science 365 (6452) (2019) 495–498.

[5] T. Zhu, Y. Liu, C. Fu, J. P. Heremans, J. G. Snyder, X. Zhao, Compromise and synergy in high-efficiency thermoelectric materials, Adv. Mater. 29 (14) (2017) 1605884.

[6] H. Shang, Z. Liang, C. Xu, S. Song, D. Huang, H. Gu, J. Mao, Z. Ren, F. Ding, N-type $Mg_3Sb_{2-x}Bi_x$ with improved thermal stability for thermoelectric power generation, Acta Mater. 201 (2020) 572–579.

[7] F. Guo, J. Zhu, B. Cui, Y. Sun, X. Zhang, W. Cai, J. Sui, Compromise of thermoelectric and mechanical properties in $LiSbTe_2$ and $LiBiTe_2$ alloyed snte, Acta Mater. 231 (2022) 117922.

[8] A. Zhang, Y. Cui, J. Yue, J. Li, Y. Pan, X. Chen, Y. Liu, T. Cui, Pressure-induced enhancement of thermoelectric performance of CoP_3 by the structural phase transition, Acta Mater. 248 (2023) 118773.

[9] C. Shen, N. Hadaeghi, H. K. Singh, T. Long, L. Fan, G. Qin, H. Zhang, Two-dimensional buckling structure induces the ultra-low thermal conductivity: a comparative study of the group GaX (X= N, P, As), J. Mater. Chem. C 10 (4) (2022) 1436–1444.

[10] J. Yue, S. Guo, J. Li, J. Zhao, C. Shen, H. Zhang, Y. Liu, T. Cui, Pressure-induced remarkable four-phonon interaction and enhanced thermoelectric conversion efficiency in $CuInTe_2$, Mater. Today Phys. (2023) 101283.

[11] G. Samsonidze, B. Kozinsky, Accelerated screening of thermoelectric materials by first-principles computations of electron–phonon scattering, Adv. Energy. Mater. 8 (20) (2018) 1800246.

[12] A. Jain, Y. Shin, K. A. Persson, Computational predictions of energy materials using density functional theory, Nat. Rev. Mater. 1 (1) (2016) 1–13.

[13] J. Yue, A. Zhang, J. Li, Y. Liu, T. Cui, Significantly reinforced thermoelectric performance in the novel 1T-Au_6Se_2 monolayer, APL Mater. 11 (3) (2023).

[14] H. Lin, G. Tan, J.-N. Shen, S. Hao, L.-M. Wu, N. Calta, C. Malliakas, S. Wang, C. Uher, C. Wolverton, et al., Concerted rattling in $CsAg_5Te_3$ leading to ultralow thermal conductivity and high thermoelectric performance, Angew. Chem. Int. Edit. 55 (38) (2016) 11431–11436.

[15] Y. Mizuguchi, A. Omachi, Y. Goto, Y. Kamihara, M. Matoba, T. Hiroi, J. Kajitani, O. Miura, Enhancement of thermoelectric properties by se substitution in layered bismuth-chalcogenide $LaOBiS_{2-x}Se_x$, J. Appl. Phys. 116 (16) (2014).

[16] A. Maignan, E. Guilmeau, F. Gascoin, Y. Bréard, V. Hardy, Revisiting some chalcogenides for thermoelectricity, Sci. Technol. Adv. Mater. (2012).

[17] Y. Zhao, S. Zeng, G. Li, C. Lian, Z. Dai, S. Meng, J. Ni, Lattice thermal conductivity including phonon frequency shifts and scattering rates induced by quartic anharmonicity in cubic oxide and fluoride perovskites, Phy. Rev. B 104 (22) (2021) 224304.

[18] C. Shen, M. Dai, X. Xiao, N. Hadaeghi, W. Xie, A. Weidenkaff, T. Tadano, H. Zhang, Impact of quartic anharmonicity on lattice thermal transport in $EuTiO_3$: A comparative theoretical and experimental investigation, Mater. Today Phys. 34 (2023) 101059.

[19] M. Lindorf, K. Mazzio, J. Pflaum, K. Nielsch, W. Brütting, M. Albrecht, Organic-based thermoelectrics, J. Mater. Chem. A 8 (16) (2020) 7495–7507.

[20] J. Chu, J. Huang, R. Liu, J. Liao, X. Xia, Q. Zhang, C. Wang, M. Gu, S. Bai, X. Shi, et al., Electrode interface optimization advances conversion efficiency and stability of thermoelectric devices, Nat. Commun 11 (1) (2020) 2723.

[21] H.-J. Pang, H. Yu, W.-J. Li, L.-C. Chen, P.-F. Qiu, Q. Peng, X.-J. Chen, Topological states of thermoelectric Yb-filled skutterudites, Phys. Rev. B 107 (12) (2023) 125202.

[22] J. Mao, J. Zhou, H. Zhu, Z. Liu, H. Zhang, R. He, G. Chen, Z. Ren, Thermoelectric properties of n-type ZrNiPb-based half-heuslers, Chem. Mater. 29 (2) (2017) 867–872.

[23] R. Yan, R. Xie, W. Xie, C. Shen, W. Li, B. Balke, S. Yoon, H. Zhang, A. Weidenkaff, Effects of doping ni on the microstructures and thermoelectric properties of co-excessive NbCoSn half-heusler compounds, ACS Appl. Mater. Inter. 13 (29) (2021) 34533–34542.

[24] M. Bilal, S. Jalali-Asadabadi, R. Ahmad, I. Ahmad, et al., Electronic properties of antiperovskite materials from state-of-the-art density functional theory, J. Chem. 2015 (2015).

[25] M.-H. Yu, L. Lewis, A. Moodenbaugh, Large magnetic entropy change in the metallic antiperovskite Mn_3GaC, J. Appl. Phys. 93 (12) (2003) 10128–10130.

[26] K. Kamishima, T. Goto, H. Nakagawa, N. Miura, M. Ohashi, N. Mori, T. Sasaki, T. Kanomata, Giant magnetoresistance in the intermetallic compound Mn_3GaC, Phys. Rev. B 63 (2) (2000) 024426.

[27] K. Asano, K. Koyama, K. Takenaka, Magnetostriction in Mn_3CuN, Appl. Phys. Lett. 92 (16) (2008).

[28] T. Shimizu, T. Shibayama, K. Asano, K. Takenaka, Giant magnetostriction in tetragonally distorted antiperovskite manganese nitrides, J. Appl. Phc.

[29] K. Takenaka, H. Takagi, Giant negative thermal expansion in Ge-doped anti-perovskite manganese nitrides, Appl. Phys. Lett. 87 (26) (2005).

[30] E. Chi, W. Kim, N. Hur, Nearly zero temperature coefficient of resistivity in antiperovskite compound $CuNMn_3$, Solid State Commun. 120 (7-8) (2001) 307–310.

[31] X. Song, Z. Sun, Q. Huang, M. Rettenmayr, X. Liu, M. Seyring, G. Li, G. Rao, F. Yin, Adjustable zero thermal expansion in antiperovskite manganese nitride, Adv. Mater. 23 (40) (2011) 4690–4694.

[32] Y. Okamoto, A. Sakamaki, K. Takenaka, Thermoelectric properties of antiperovskite calcium oxides Ca_3PbO and Ca_3SnO, J. Appl. Phys. 119 (20) (2016).

[33] Y. Zhao, C. Lian, S. Zeng, Z. Dai, S. Meng, J. Ni, Anomalous electronic and thermoelectric transport properties in cubic Rb_3AuO antiperovskite, Phys. Rev. B 102 (9) (2020) 094314.

[34] M. Ochi, K. Kuroki, Comparative first-principles study of antiperovskite oxides and nitrides as thermoelectric material: multiple dirac cones, low-dimensional band dispersion, and high valley degeneracy, Phys. Rev. Appl. 12 (3) (2019) 034009.

[35] A. Basit, S. A. Khan, G. Murtaza, A. Mehmood, R. Khenata, S. B. Omran, M. Yaseen, Electronic, optical and thermoelectric properties of $XNMg_3$ (X= P, As, Sb, Bi) compounds, Mat. Sci. Semicon. Proc. 43 (2016) 69–74.

[36] P. Sreedevi, R. Vidya, P. Ravindran, Antiperovskite materials as promising candidates for efficient tandem photovoltaics: First-principles investigation, Mat. Sci. Semicon. Proc. 147 (2022) 106727.

[37] K. N. Heinselman, S. Lany, J. D. Perkins, K. R. Talley, A. Zakutayev, Thin film synthesis of semiconductors in the Mg-Sb-N materials system, Chem. Mater. 31 (21) (2019) 8717–8724.

[38] D. T. Morelli, G. A. Slack, High lattice thermal conductivity solids, in: High thermal conductivity materials, Springer, 2006, pp. 37–68.

[39] Z. Chen, X. Zhang, S. Lin, L. Chen, Y. Pei, Rationalizing phonon dispersion for lattice thermal conductivity of solids, Natl. Sci. Rev. 5 (6) (2018) 888–894.

[40] G. J. Snyder, M. T. Agne, R. Gurunathan, Thermal conductivity of complex materials, Natl. Sci. Rev. 6 (3) (2019) 380–381.

[41] S. Zeng, X. Yan, Q. Shen, Y. Tu, H. Huang, G. Li, Low lattice thermal conductivities and good thermoelectric performance of hexagonal antiperovskites X(Ba & Sr)$_3$BiN with quartic anharmonicity, Phys. Chem. Chem. Phys. 25 (39) (2023) 26507–26514.

[42] R. A. Cowley, Anharmonic crystals, Rep. Prog. Phys. 31 (1) (1968) 123.

[43] A. Romero, E. Gross, M. Verstraete, O. Hellman, Thermal conductivity in pbte from first principles, Phys. Rev. B 91 (21) (2015) 214310.

[44] Y. Xia, K. Pal, J. He, V. Ozoliņš, C. Wolverton, Particlelike phonon propagation dominates ultralow lattice thermal conductivity in crystalline Tl_3VSe_4, Phys. Rev. Lett. 124 (6) (2020) 065901.

[45] M. Simoncelli, N. Marzari, F. Mauri, Unified theory of thermal transport in crystals and glasses, Nat. Phys. 15 (8) (2019) 809–813.

[46] Y. Zhu, Y. Xia, Y. Wang, Y. Sheng, J. Yang, C. Fu, A. Li, T. Zhu, J. Luo, C. Wolverton, et al., Violation of the T^{-1} relationship in the lattice thermal conductivity of Mg_3Sb_2 with locally asymmetric vibrations, Research (2020).

[47] G. Kresse, J. Furthmüller, Efficient iterative schemes for ab initio total-energy calculations using a plane-wave basis set, Phys. Rev. B 54 (16) (1996) 11169.

[48] G. Kresse, D. Joubert, From ultrasoft pseudopotentials to the projector augmented-wave method, Phys. Rev. B 59 (3) (1999) 1758.

[49] G. I. Csonka, J. P. Perdew, A. Ruzsinszky, P. H. Philipsen, S. Lebègue, J. Paier, O. A. Vydrov, J. G. Ángyán, Assessing the performance of recent density functionals for bulk solids, Phys. Rev. B 79 (15) (2009) 155107.

[50] S. Kirklin, J. E. Saal, B. Meredig, A. Thompson, J. W. Doak, M. Aykol, S. Rühl, C. Wolverton, The open quantum materials database (oqmd): assessing the accuracy of dft formation energies, Npj Compu. Mater. 1 (1) (2015) 1–15.

[51] F. Zhou, B. Sadigh, D. Åberg, Y. Xia, V. Ozoliņš, et al., Compressive sensing lattice dynamics. ii. efficient phonon calculations and long-range interactions, Phys. Rev. B 100 (18) (2019) 184309.

[52] T. Tadano, Y. Gohda, S. Tsuneyuki, Anharmonic force constants extracted from first-principles molecular dynamics: applications to heat transfer simulations, J. Phys-Condens. Mat. 26 (22) (2014) 225402.

[53] T. Feng, X. Ruan, Quantum mechanical prediction of four-phonon scattering rates and reduced thermal conductivity of solids, Phys. Rev. B 93 (4) (2016) 045202.

[54] Z. Han, X. Yang, W. Li, T. Feng, X. Ruan, Fourphonon: An extension module to shengbte for computing four-phonon scattering rates and thermal conductivity, Compu. Phys. Commun. 270 (2022) 108179.

[55] A. M. Ganose, J. Park, A. Faghaninia, R. Woods-Robinson, K. A. Persson, A. Jain, Efficient calculation of carrier scattering rates from first principles, Nat. Commun. 12 (1) (2021) 2222.

[56] T. A. Manz, N. G. Limas, Introducing ddec6 atomic population analysis: part 1. charge partitioning theory and methodology, RSC Adv. 6 (53) (2016) 47771–47801.

[57] N. G. Limas, T. A. Manz, Introducing ddec6 atomic population analysis: part 2. computed results for a wide range of periodic and nonperiodic materials, RSC Adv. 6 (51) (2016) 45727–45747.

[58] T. A. Manz, Introducing DDEC6 atomic population analysis: part 3. comprehensive method to compute bond orders, RSC Adv. 7 (72) (2017) 45552–45581.

[59] Y. Wang, H. Zhang, J. Zhu, X. Lü, S. Li, R. Zou, Y. Zhao, Antiperovskites with exceptional functionalities, Adv. Mater. 32 (7) (2020) 1905007.

[60] Z.-y. Gao, W. Wang, B.-c. Li, L. Sun, F. Wang, Potential antiperovskite semiconductor compounds Mg_3XN (X= P, As, Sb, Bi): the first-principles study, J. Supercond. Nov. Magn. 35 (11) (2022) 3277–3290.

[61] K. Amara, M. Zemouli, M. Elkeurti, A. Belfedal, F. Saadaoui, First-principles study of $XNMg_3$ (X= P, As, Sb and Bi) antiperovskite compounds, J. Alloy. Compd. 576 (2013) 398–403.

[62] E. Chi, W. Kim, N. Hur, D. Jung, New Mg-based antiperovskites $PnNMg_3$ (Pn= As, Sb), Solid state commun. 121 (6-7) (2002) 309–312.

[63] C. Shen, Q. Gao, N. M. Fortunato, H. K. Singh, I. Opahle, O. Gutfleisch, H. Zhang, Designing of magnetic MAB phases for energy applications, J. Mater. Chem. A 9 (13) (2021) 8805–8813.

[64] S. Nosé, A unified formulation of the constant temperature molecular dynamics methods, J. Chem. phys. 81 (1) (1984) 511–519.

[65] M. Born, K. Huang, M. Lax, Dynamical theory of crystal lattices, Am. J. Phys. 23 (7) (1955) 474–474.

[66] F. Mouhat, F.-X. Coudert, Necessary and sufficient elastic stability conditions in various crystal systems, Phys. Rev. B 90 (22) (2014) 224104.

[67] H. Zhong, C. Feng, H. Wang, D. Han, G. Yu, W. Xiong, Y. Li, M. Yang, G. Tang, S. Yuan, Structure–composition–property relationships in antiperovskite nitrides: guiding a rational alloy design, ACS Appl. Mater. Interfaces 13 (41) (2021) 48516–48524.

[68] S. Pugh, Xcii. relations between the elastic moduli and the plastic properties of polycrystalline pure metals, The London, Edinburgh, and Dublin Philosophical Magazine and Journal of Science 45 (367) (1954) 823–843.

[69] Y. Luo, J. Wang, Y. Li, J. Wang, Giant phonon anharmonicity and anomalous pressure dependence of lattice thermal conductivity in $Y_2Si_2O_7$ silicate, Sci. Rep. 6 (1) (2016) 29801.

[70] D. Yang, W. Yao, Y. Yan, W. Qiu, L. Guo, X. Lu, C. Uher, X. Han, G. Wang, T. Yang, et al., Intrinsically low thermal conductivity from a

quasi-one-dimensional crystal structure and enhanced electrical conductivity network via pb doping in $SbCrSe_3$, NPG Asia Mater. 9 (6) (2017) e387–e387.

[71] J. Zheng, D. Shi, Y. Yang, C. Lin, H. Huang, R. Guo, B. Huang, Anharmonicity-induced phonon hardening and phonon transport enhancement in crystalline perovskite $BaZrO_3$, Phys. Rev. B 105 (22) (2022) 224303.

[72] Y. Mochizuki, H.-J. Sung, A. Takahashi, Y. Kumagai, F. Oba, Theoretical exploration of mixed-anion antiperovskite semiconductors M_3XN (M= Mg, Ca, Sr, Ba; X= P, As, Sb, Bi), Phys. Rev. Mater. 4 (4) (2020) 044601.

[73] V. M. Goldschmidt, Die gesetze der krystallochemie, NATURWISSENSCHAFTEN 14 (21) (1926) 477–485.

[74] T. Tadano, S. Tsuneyuki, Self-consistent phonon calculations of lattice dynamical properties in cubic $SrTiO_3$ with first-principles anharmonic force constants, Phys. Rev. B 92 (5) (2015) 054301.

[75] T. Tadano, W. A. Saidi, First-principles phonon quasiparticle theory applied to a strongly anharmonic halide perovskite, Phys. Rev. L 129 (18) (2022) 185901.

[76] J. Zheng, C. Lin, C. Lin, R. Guo, B. Huang, Strong anharmonic phonon renormalization and dominant role of wave-like tunnelling of phonons in thermal transport in lead-free halide double perovskites, arXiv preprint arXiv:2301.12273 (2023).

[77] X. Song, Y. Zhao, J. Ni, S. Meng, Z. Dai, High thermoelectric performance in $XAgSe_2$ (X= Sc, Y) from strong quartic anharmonicity and multi-valley band structure, J. Mater. Chem. A (2023).

[78] J. Feldman, D. Singh, I. Mazin, D. Mandrus, B. Sales, Lattice dynamics and reduced thermal conductivity of filled skutterudites, Phys. Rev. B 61 (14) (2000) R9209.

[79] W. Li, N. Mingo, Thermal conductivity of fully filled skutterudites: Role of the filler, Phys. Rev. B 89 (18) (2014) 184304.

[80] J. He, M. Amsler, Y. Xia, S. S. Naghavi, V. I. Hegde, S. Hao, S. Goedecker, V. Ozoliņš, C. Wolverton, Ultralow thermal conductivity in full heusler semiconductors, Phys. Rev. Lett. 117 (4) (2016) 046602.

[81] W. Li, N. Mingo, Ultralow lattice thermal conductivity of the fully filled skutterudite $YbFe_4Sb_{12}$ due to the flat avoided-crossing filler modes, Phys. Rev. B 91 (14) (2015) 144304.

[82] X. Song, Y. Zhao, J. Ni, S. Meng, Z. Dai, Thermal transport properties of anisotropic materials RbCaX (X= As, Sb) with strong anharmonicity, Comp. Mater. Sci. 213 (2022) 111618.

[83] X. Song, Y. Zhao, J. Ni, S. Meng, Z. Dai, Strong anharmonic phonon scattering and superior thermoelectric properties of Li_2NaBi, Mater. Today Phys. 31 (2023) 100990.

[84] Z. Tian, J. Garg, K. Esfarjani, T. Shiga, J. Shiomi, G. Chen, Phonon conduction in pbse, pbte, and $PbTe_{1-x}Se_x$ from first-principles calculations, Phys. Rev. B 85 (18) (2012) 184303.

[85] N. K. Ravichandran, D. Broido, Phonon-phonon interactions in strongly bonded solids: selection rules and higher-order processes, Phys. Rev. X 10 (2) (2020) 021063.

[86] Y. Zhao, S. Zeng, G. Li, C. Lian, Z. Dai, S. Meng, J. Ni, Lattice thermal conductivity including phonon frequency shifts and scattering rates induced by quartic anharmonicity in cubic oxide and fluoride perovskites, Phys. Rev. B 104 (22) (2021) 224304.

[87] K. Brlec, K. B. Spooner, J. M. Skelton, D. O. Scanlon, $Y_2Ti_2O_5S_2$–a promising n-type oxysulphide for thermoelectric applications, J. Mater. Chem. A 10 (32) (2022) 16813–16824.

[88] Y. Mochizuki, H.-J. Sung, A. Takahashi, Y. Kumagai, F. Oba, Theoretical exploration of mixed-anion antiperovskite semiconductors M_3XN (M= Mg, Ca, Sr, Ba; X= P, As, Sb, Bi), Phys. Rev. Mater. 4 (4) (2020) 044601.

[89] A. E. van Arkel, J. Swallow, Molecules and crystals in inorganic chemistry, Butterworths London, 1956.

[90] W. Sun, C. J. Bartel, E. Arca, S. R. Bauers, B. Matthews, B. Orvañanos, B.-R. Chen, M. F. Toney, L. T. Schelhas, W. Tumas, et al., A map of the inorganic ternary metal nitrides, Nat. Mater. 18 (7) (2019) 732–739.

[91] M. Wuttig, V. L. Deringer, X. Gonze, C. Bichara, J.-Y. Raty, Incipient metals: functional materials with a unique bonding mechanism, Adv. Mater. 30 (51) (2018) 1803777.

[92] W. Cao, Z. Wang, L. Miao, J. Shi, R. Xiong, Extremely anisotropic thermoelectric properties of SnSe under pressure, Energy Environ. Mater. 6 (3) (2023) e12361.

[93] J. H. Fetherolf, P. Shih, T. C. Berkelbach, Conductivity of an electron coupled to anharmonic phonons: Quantum-classical simulations and comparison of approximations, Phys. Rev. B 107 (6) (2023) 064304.

[94] K.-C. Zhang, C. Shen, H.-B. Zhang, Y.-F. Li, Y. Liu, Effect of quartic anharmonicity on the carrier transport of cubic halide perovskites $CsSnI_3$ and $CsPbI_3$, Phys. Rev. B 106 (23) (2022) 235202.

[95] A. Lavasani, D. Bulmash, S. D. Sarma, Wiedemann-franz law and fermi liquids, Phys. Rev. B 99 (8) (2019) 085104.